Contents lists available at ScienceDirect

Nuclear Inst. and Methods in Physics Research, A

journal homepage: www.elsevier.com/locate/nima

Full Length Article

High-precision 4D tracking with large pixels using thin resistive silicon detectors

R. Arcidiacono [a,b,*], G. Borghi [d], M. Boscardin [e], N. Cartiglia [a], M. Centis Vignali [e], M. Costa [c], G-F. Dalla Betta [f], M. Ferrero [a], F. Ficorella [e], G. Gioachin [c], L. Lanteri [c], M. Mandurrino [a], L. Menzio [a], R. Mulargia [a,c], L. Pancheri [f], G. Paternoster [e], A. Rojas [a], H-F.W. Sadrozinski [g], A. Seiden [g], F. Siviero [a], V. Sola [a,c], M. Tornago [a,c]

[a] *INFN, Sezione di Torino, Italy*
[b] *Università del Piemonte Orientale, Italy*
[c] *Università di Torino, Torino, Italy*
[d] *Politecnico di Milano, Milano, Italy*
[e] *Fondazione Bruno Kessler, Trento, Italy*
[f] *Università degli Studi di Trento, Trento, Italy*
[g] *University of California at Santa Cruz, CA, USA*

ARTICLE INFO

ABSTRACT

The basic principle of operation of silicon sensors with resistive read-out is built-in charge sharing. Resistive Silicon Detectors (RSD, also known as AC-LGAD), exploiting the signals seen on the electrodes surrounding the impact point, achieve excellent space and time resolutions even with very large pixels. In this paper, a TCT system using a 1064 nm picosecond laser is used to characterize RSD sensors produced by Fondazione Bruno Kessler. The paper first introduces the parametrization of the errors in the determination of the position and time coordinates in RSD, then outlines the reconstruction method, and finally presents the results. Three different pixel pitches are used in the analysis: 200×340, 450×450, and 1300×1300 μm². At gain = 30, the 450×450 μm² pixel achieves a time jitter of 20 ps and a spatial resolution of 15 μm concurrently, while the 1300×1300 μm² pixel achieves 30 ps and 30 μm, respectively. The implementation of cross-shaped electrodes improves considerably the response uniformity over the pixel surface.

1. Introduction

High-precision tracking requires the concurrent minimization of two quantities: (i) the hit position resolution $\sigma_{hit\ pos}$, how precisely the impact point is located on the sensor surface, and (ii) the multiple scattering position resolution σ_{MS}, how much the tracker materials (cables, cooling, mechanics, the detector itself) influence the determination of the hit position.

The two terms, $\sigma_{hit\ pos}$ and σ_{MS}, are deeply linked to each other and to the type of read-out architecture (single pixel or multi-pixel) used in the system.

In single-pixel read-out, shown in Fig. 1(A), the hit resolution $\sigma_{hit\ pos}$ is the standard deviation of a uniform random variable distributed over the pixel size, $\sigma_{hit\ pos} = k * pixel\ size/\sqrt{12}$, where $k \sim 0.5 - 1$. This relationship is at the root of the limited spatial accuracy achievable with single-pixel read-out: the pixel size determines the spatial resolution. Only tiny pixels (25×25 μm²) achieve a precision of

5–10 μm, and it is practically impossible to reach smaller pitches. The small pixel size results in many pixels and read-out channels, which leads to large power consumption.

In multi-pixel read-out, shown in Fig. 1(B), the signal is split between two (or possibly more) pixels, and the position of a hit can be calculated as the signal-weighted centroid (or a similar algorithm) of the coordinates of the two pixels. This method is robust and reaches excellent accuracy, yielding $\sigma_{hit\ pos}$ significantly smaller than $k * pixel\ size/\sqrt{(12)}$. However, to maintain full detection efficiency with shared signals, thick sensors are needed, to generate large enough charge. When signal sharing is obtained exploiting the tracker magnetic field, Fig. 1 (B), the sensor needs to be even thicker (200–300 μm) to allow sufficient bending of the drift lines.

As two examples of these approaches, the ATLAS experiment has used a vertex tracker with small pixels and a single-pixel read-out (50×400 μm² pixels and $\sigma_{hit\ pos} = 10$ μm on the small side) [1] while

---

* Corresponding author at: INFN, Sezione di Torino, Italy.
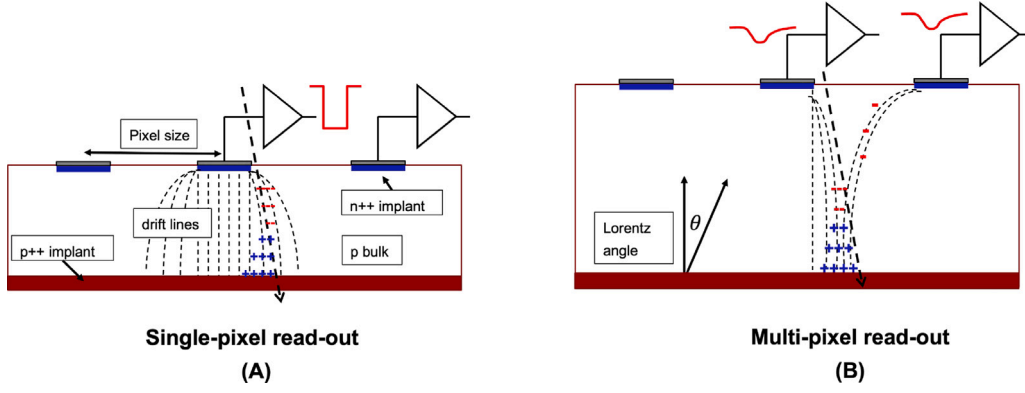 *E-mail address:* arcidiacono@to.infn.it (R. Arcidiacono).

Fig. 1. (A) Single and (B) multi-pixel read-out schemes for silicon sensors. The presence of a magnetic field modifies the drift line adding a Lorentz angle that induces charge sharing between two adjacent pads.
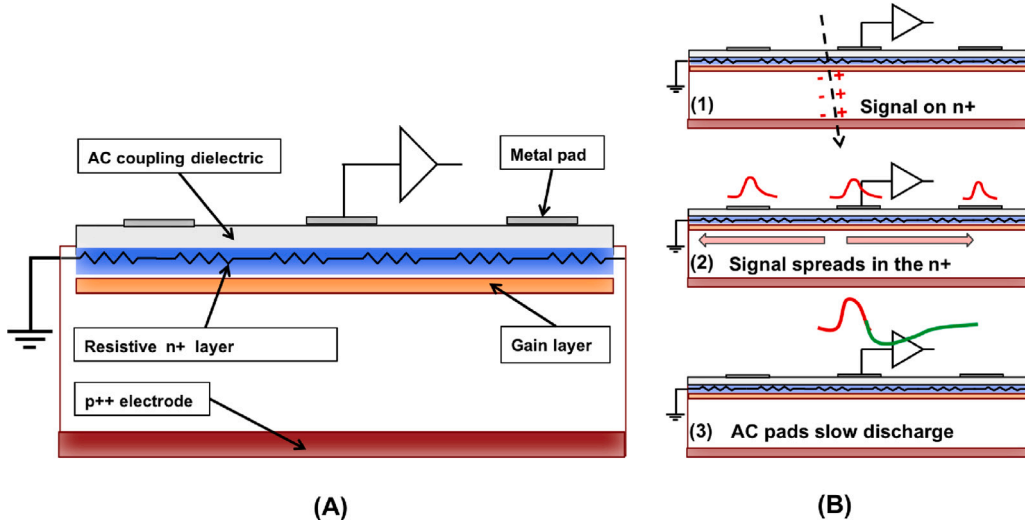

Fig. 2. (A) Sketch of an RSD. The main components are indicated in the sketch. (B) The three phases of signal formation in RSDs.

the CMS experiment has chosen larger pixels and a multi-pixel read-out with thick sensors, exploiting the strong magnetic field present in the tracker region of the experiment (100×150 μm^2 pixels and $\sigma_{hit\ pos} = 10$ μm, 3.8 T magnet) to obtain charge sharing and improved determination of the hit position [2].

The very mechanism that optimizes $\sigma_{hit\ pos}$ is detrimental to σ_{MS}: thick sensors, necessary for signal sharing, cause significant multiple scattering and deteriorate the overall accuracy of the tracking system. In this paper, the performance of Resistive Silicon Detectors (RSD) is presented, and the results demonstrate that this novel design minimizes at the same time $\sigma_{hit\ pos}$ and σ_{MS}, while using large pixels, a key feature to significantly reduce the number of read-out channels and, in many applications, power consumption.

2. RSD principles of operation

RSDs are thin silicon sensors that combine two design innovations [3]: (i) built-in signal sharing due to the presence of resistive read-out and (ii) internal gain due to the adoption of the low-gain avalanche diode design. Fig. 2(A) shows a sketch of the RSD design, while Fig. 2(B) outlines the working principles: (1) the drift of the e/h pairs generates an induced signal on the n$^+$ resistive layer, the signal is amplified by the presence of an internal gain mechanism; (2) the signal spreads toward the ground in the n$^+$ resistive layer; the fast component of the signal is visible on the AC metal pads as they offer the lowest impedance high-frequency paths to ground; (3) the AC pads discharge

with a time constant that depends on the read-out input resistance, the n$^+$ sheet resistance, and the system capacitance.

The signal splits among the read-out pads like a current in an impedance divider, where the impedance is that of the paths connecting the impact point to each of the read-out pads, as sketched in Fig. 3.

3. Parametrization of the spatial resolution of RSD

There are four distinct contributions to the spatial resolution, listed in Eq. (1):

$$\sigma_{hit\ pos}^2 = \sigma_{jitter}^2 + \sigma_{rec}^2 + \sigma_{setup}^2 + \sigma_{sensor}^2. \tag{1}$$

The first contribution, σ_{jitter}, degrades the precision of the measurement, while the other terms degrade the accuracy.

- σ_{jitter}: this term is related to the electronic noise $\sigma_{el-noise}$. As illustrated in Fig. 4, the variation of signal amplitude due to the electronic noise induces uncertainty in the hit localization given by

$$\sigma_{jitter} = \sigma_{el-noise}/(dV/dx) \sim \frac{\sigma_{el-noise}}{Amplitude} \times pixel\ size, \tag{2}$$

where dV/dx depends upon the signal amplitude and pixel size. In the examples shown in Fig. 4, the amplitude changes by dV/dx = 0.15 (0.05) mV/μm for a 450 (1300) μm pixel. Assuming $\sigma_{el-noise} \sim 2$ mV, the jitter term is about $\sigma_{jitter} \sim 13$ μm for a 450 μm pixel, while it becomes $\sigma_{jitter} \sim 40$ μm for 1300 μm pixels.
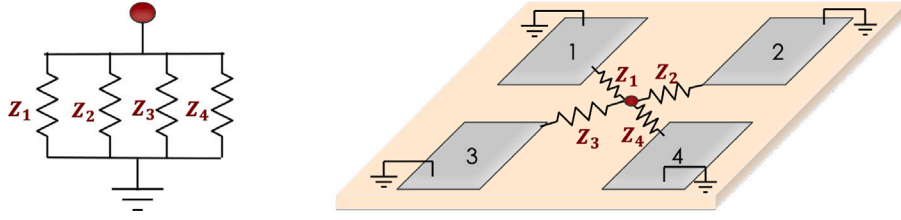
Fig. 3. In RSD, the signal splits among the read-out pads like a current in an impedance divider.
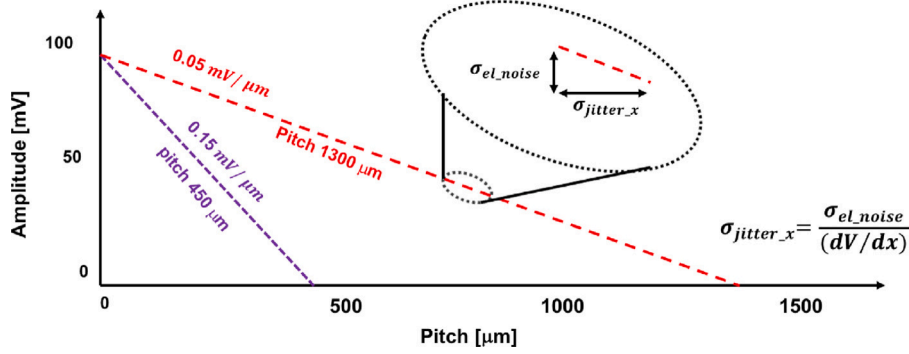

Fig. 4. Amplitude as a function of distance for two RSD geometries (qualitative trend). In large structures, the decrease of the signal per micron is smaller, leading to a larger the jitter term.

If the signal is uniformly split among n read-out channels, the amplitude seen on each pad is actually $1/n$ smaller, while the effective noise is reduced by $\sqrt{n}$ due to the combination of the signals from the n read-out pads:

$$\sigma_{jitter} \sim \frac{\frac{\sigma_{el-noise}}{\sqrt{n}}}{\frac{dV/dx}{n}} = \frac{\sigma_{el-noise}}{dV/dx}\sqrt{n}. \tag{3}$$

As seen in this paragraph, the electronic noise sets the limit of the spatial precision, and for equal noise, the precision depends linearly on the pixel size. If high spatial precision with large pixels is needed, then the electronics should be very low noise and the signal gain large enough.

- σ_{rec}: the reconstruction code uses algorithms to infer the hit position from the measured signals. This can be done in several ways: analytically, using methods based on look-up tables, or with more advanced techniques such as machine learning. In all methods, the reconstructed hit positions might have a position-dependent systematic offset with respect to the true position.
- σ_{setup}: this term includes the uncertainties related to the experimental set-up. Specifically, the most important are those effects that change the relative amplitude between the actual signal sharing and the measured signal sharing (for example, differences in the amplifier gain used to read out the electrodes).
- σ_{sensor}: this term groups all sensor imperfections contributing to an uneven signal sharing among pads. The most obvious one is a varying n^+ resistivity: a 2% difference in n^+ resistivity corresponds to an equal amplitude imbalance between two pads, yielding a shift of the position assignment of ~ 7 µm for a 450 µm geometry and of 20 µm for a 1300 µm pixel. The uniformity of the n^+ resistive layer (and that of the gain implant) is a crucial parameter in RSD optimized for micron-level position resolution.

4. Parametrization of the time resolution of RSD

The parametrization expressing the time resolution of a single read-out pad is similar to that of a standard Ultra-Fast Silicon Detector (UFSD) [4]. In RSD, there is an additional contribution due to the uncertainty in the determination of the signal delay, i.e. the time interval between the hit time and when the signal is visible on the read-out pad.

$$\sigma^2_{hit\ time} = \sigma^2_{jitter} + \sigma^2_{Landau} + \sigma^2_{delay} \tag{4}$$

- σ_{jitter}: due to the electronics, $\sigma_{jitter} = \sigma_{el-noise}/(dV/dt)$
- σ_{Landau}: due to non-uniform ionization. Assuming a 50 µm thick sensor, this term is about 30 ps.
- σ_{delay}: due to the uncertainty on the hit position reconstruction.

Overall, a good time resolution requires large signals, low noise electronics, thin sensors, and a good determination of the impact point.

In RSDs, the time resolution is limited by the time jitter term for small signals, and by the Landau noise for large signals, while it is not degraded significantly by moderate sensor non-uniformity, or by an uncertainty in the hit position of the order of 30–40 µm, which would lead to a miscalculation of the delay time by only 10–30 ps (the propagation depends on surface resistivity and sensor capacitance, see also Section 7.2).

If the n^+ resistivity is low, and the delay is well measured, the time resolution does not depend significantly on the pixel size. As for the spatial case, see Eq. (3), σ_{jitter} increases when splitting the signal on n read-out pads as $\sigma_{jitter} \propto \sqrt{n}$.

5. The second RSD production (RSD2) at Fondazione Bruno Kessler

The studies performed using the first production of resistive silicon detectors [5] (RSD1), manufactured at Fondazione Bruno Kessler (FBK), have shown that signal sharing can be optimized by a careful design of the read-out electrode shape [3,6]. The electrodes need to surround as much as possible the pixel area to confine the signal spread to a predefined number of pads, and the metal of the electrodes needs to be minimized to achieve a uniform response over the pixel area. The RSD2 production includes several optimizations of the electrode shapes [7], a few examples are shown in Fig. 5. A two-electrodes configuration (A) is particularly suited when only one of the two coordinates needs to be known precisely, for example, in the measurements of the trajectory of a particle in a magnetic field. Configurations (B) and (C) split the signal respectively among three or four electrodes, with (C) sharing it more
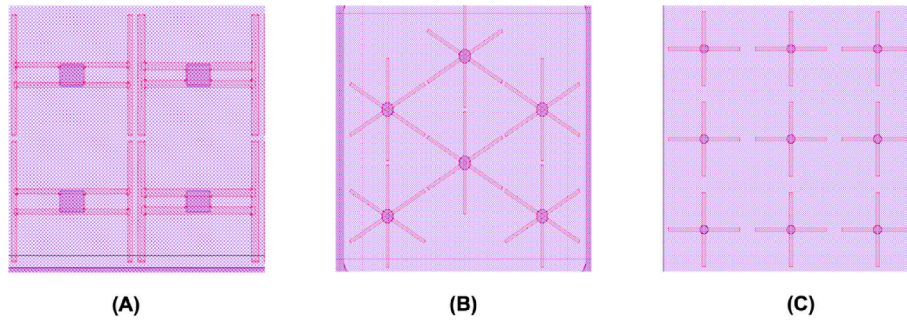
Fig. 5. (A) 2-pixel sharing: this configuration is useful when only one coordinate needs to be determined accurately (B) 3-pixel sharing: the electrodes are at the vertexes of a triangle, with arms extending out. (C) 4-pixel sharing: the electrodes are placed at the vertexes of a square.

Table 1
List of devices used in this analysis. The three structures use the cross-shaped electrodes shown in Fig. 5(C).

Version	Device [μm²]	Pixel [μm²]	Contact pad [μm]	Arm width [μm]	Gap between arms [μm]
V1	800 × 800	200 × 345	30	10	5
V2	2700 × 2700	450 × 450	45	20	10
V3	2700 × 2700	1300 × 1300	90	20	100

uniformly due to a larger angle between the electrode arms. For each of these configurations, several design variations have been implemented in RSD2, changing the arm width, the distance between arms, and the size of the contact pad. These aspects impact the electrode capacitance, the shape of the signal, and the capability of limiting the signal spread outside the pixel area.

The analysis presented in this paper uses three different versions of the type shown in Fig. 5 (C), listed in Table 1. The active thickness of all RSD productions from FBK is 50 μm.

6. The experimental set-up

The present studies have been performed with a high-precision Transient Current Technique (TCT) set-up [8]. In this set-up, a 1064 nm laser with pulses as short as 50 ps, generates e/h pairs in the sensor under test, emulating the passage of a minimum ionizing particle. The diameter of the laser spot has been measured to be in the 5–10 μm range, depending on the precision of the calibration procedure. The sensors were tested using a 16-channel read-out board designed at Fermilab (the so-called FNAL board). Each read-out channel consists of a 2-stage amplifier chain based on the Mini-Circuits GALI-66+ integrated circuit with a 25 Ω input resistance, a ~5 kΩ total transimpedance, and a bandwidth of 1 GHz [9], which does not modify the shape of the signal. The amplified signals were then recorded for offline analyses by a fast digitizer (16-channel CAEN DT5742, with a 5 GS/s sampling rate). The noise of the system, as measured using empty events, was evaluated to be $\sigma_{el-noise} = 1.04$ mV. In the position and time reconstruction of the events, only the signals collected on four read-out pads at the corners of the pixel under study were used.

A key point when using the TCT set-up is the calibration of the laser intensity. Since the performance of the FNAL board are very well measured, the laser intensity has been monitored by measuring the area of the signal generated on the n^+ resistive layer, read out via a pad in contact with the layer (so-called DC electrode), knowing that a signal area of 5 pWb (V · s over a 50 ohm resistance) corresponds to about 1 fC of charge. Using this calibration and the gain-bias characteristics (see Section 8) of the sensor under study previously measured, it is straightforward to set the laser intensity so that it generates a 1-MIP equivalent charge.

7. The reconstruction method

In RSDs, the way the signal is shared among the read-out electrodes depends upon the relative distances between the impact point and the read-out electrodes. For this reason, the position of the impact point can be identified using the measured signal sharing. For specific electrode layouts, such as the one shown in Fig. 6(A), the distance between the hit position and each of the pads is uniquely identified. In this configuration, it is possible to calculate the signal split and delays, as performed in [3], and infer the position of the impact point by comparing the measured and calculated signal sharing. On the other hand, for layouts with extended electrodes, like the one shown in Fig. 6(B), the analytic approach does not model well enough the propagation on the resistive layer. The signal on a given pad is, in this case, the sum of many contributions, each following a different path. For such layouts, an efficient approach is to identify an appropriate reconstruction algorithm and then correct its biases by measuring them experimentally.

7.1. Reconstruction of the hit position

The first step in the position determination for the case of Fig. 6(B) is to define the reconstruction algorithms. For this analysis, two different algorithms were considered: (i) the Signal-Weighted Position (SWP), and (ii) the Discretized Position Circuit (DPC) [10].

The SWP equations are:

$$x_{meas} = \frac{\sum_i^4 x_i * A_i}{\sum_i^4 A_i}$$
$$y_{meas} = \frac{\sum_i^4 y_i * A_i}{\sum_i^4 A_i}, \tag{5}$$

where x_{meas}, y_{meas} are the hit coordinates, x_i, y_i the coordinates of the pads central points, and A_i the signal measured on pad i.

In DPC, the position is reconstructed using the signal imbalance between the two sides (right - left, top - bottom) of the pixel, as shown in Eq. (6):

$$x_{meas} = x_0 + k_x * \frac{(A_3 + A_4) - (A_1 + A_2)}{A_1 + A_2 + A_3 + A_4}$$
$$y_{meas} = y_0 + k_y * \frac{(A_1 + A_3) - (A_2 + A_4)}{A_1 + A_2 + A_3 + A_4}, \tag{6}$$
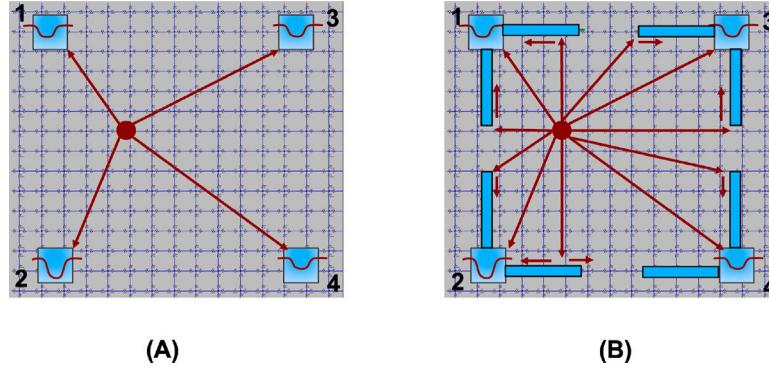
Fig. 6. Sketch of signal sharing for two RSD with different layouts of the read-out electrodes. (A) a layout with point-like electrodes. (B) a layout with extended electrodes. An analytic formulation of the sharing mechanism for (B) is difficult to be achieved due to the presence of multiple current paths leading to the same read-out electrode.
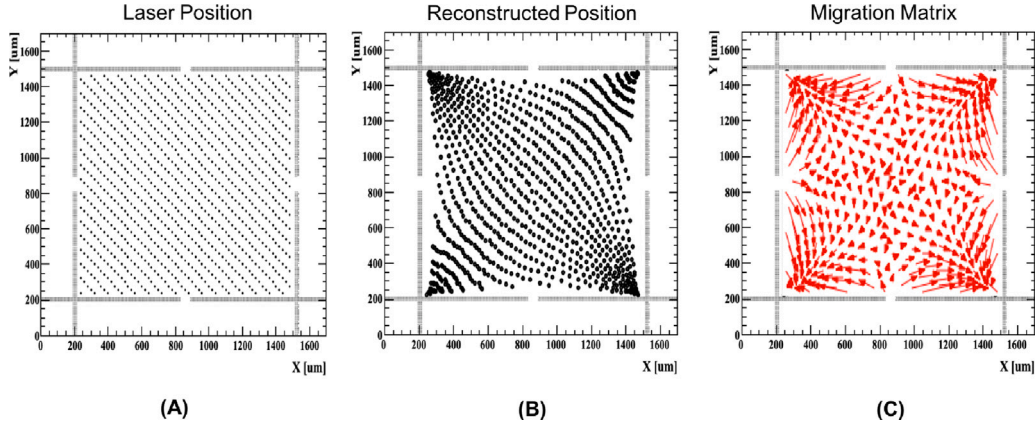

Fig. 7. Determination of the migration map (for DPC using amplitude) for a $1300 \times 1300 \ \mu m^2$ pixel: (A) map of the laser positions on the pixel, (B) map of the reconstructed positions, (C) migration map obtained connecting the true positions with the reconstructed positions.

where A_i is the signal measured on the pad i, x_0, y_0 are the coordinates of the central point of the pixel, and k_x, k_y are given by:

$$k_x = \frac{pixel\ size}{2} * \frac{1}{\frac{(A_3+A_4)-(A_1+A_2)}{A_1+A_2+A_3+A_4}\big|_{x=x_3}}$$
$$k_y = \frac{pixel\ size}{2} * \frac{1}{\frac{(A_1+A_3)-(A_2+A_4)}{A_1+A_2+A_3+A_4}\big|_{y=y_3}}. \tag{7}$$

The coefficients k_x, k_y are measured experimentally and account for the fact that if the hit point is on one side of the pixel (at $x = x_3$ to determine k_x and at $y = y_3$ to determine k_y), the signals measured on the read-out pads on the other side might not be equal to zero. This is especially important in small pixels: in that case, if k_x, k_y are set to 1, the reconstruction algorithm clusters the hit positions toward the center of the pixel.

The quantity A_i in both SWP and DPC can be either the amplitude or the integral of the signal (signal area). One important difference between the two quantities is that the amplitude of a signal decreases during the propagation on the n^+ resistive layer while the area does not change.

Amplitudes, therefore, carry more information and potentially lead to a better resolution. Ultimately, the decision to use amplitudes or integrals of the signals depends on the type of electronics used, i.e., on the signal-to-noise ratios of the two choices.

7.1.1. Accuracy of the reconstruction methods

The next step is to evaluate the accuracy of the reconstruction methods (SWP and DPC), i.e. to measure by how much the measured coordinates (x_{meas}, y_{meas}) differ systematically from the true hit coordinates (x_{true}, y_{true}). This step is performed by collecting data, called in the following "training data", with the TCT set-up.

In each acquisition sequence, the laser moves by 10 or 20 μm covering the whole Detector Under test (DUT) surface, and for each position, 100 shots are recorded. The hit positions are then reconstructed either using SWP or DPC and compared with the true coordinates. Fig. 7 shows an example of this process: (A) map of the laser positions covering the surface of the pixel (B) map of the reconstructed positions (C) the migration map obtained connecting the true positions with the reconstructed positions: it represents graphically the offset associated to each point.

The position reconstruction, shown in (B), is already fairly accurate thanks to the cross-shaped design of the metal electrodes. The largest migration is concentrated in the corners and near the metal arms: in these regions, the reconstruction clusters the points toward the closest read-out pad.

7.1.2. Use of signal area or signal amplitude, SWP or DPC

The amplitude of the signal is obtained by fitting a gaussian to the three or four highest samples around the signal peak, while the area is obtained by summing the areas of these bins. Since the clock in the digitizer is not synchronized to the laser trigger, these highest samples are not at fixed positions with respect to the signal peak. This fact introduces a large uncertainty in the determination of the signal area preventing further its use in the analysis. For this reason, in the following part of this paper, only the signal amplitude is used with both the DPC and SWP methods.

Fig. 8 reports the measurement accuracies, defined as the mean difference between the true and reconstructed positions over the whole DUT, of the two reconstruction methods, as a function of the pixel size. Thanks to the possibility of tuning the $k_{x,y}$ parameters, the DPC method yields better results. For the largest pitch, 1300 μm, the two methods
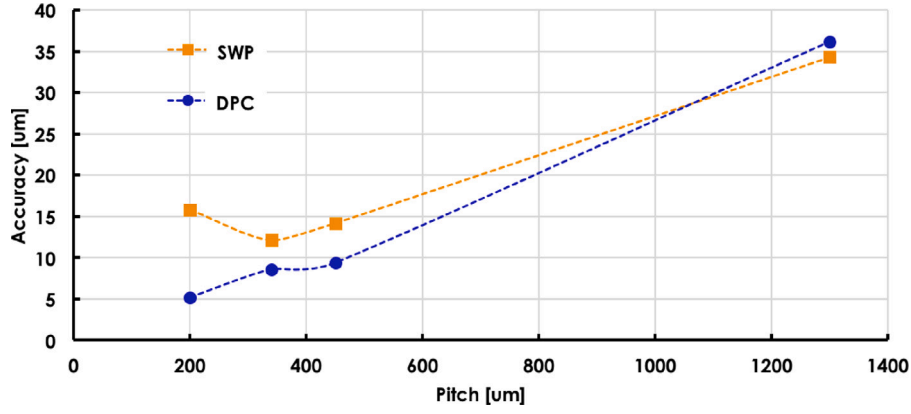
Fig. 8. The measured accuracy for the two reconstruction methods (DPC and SWP) as a function of the pitch size (migration matrix not applied).
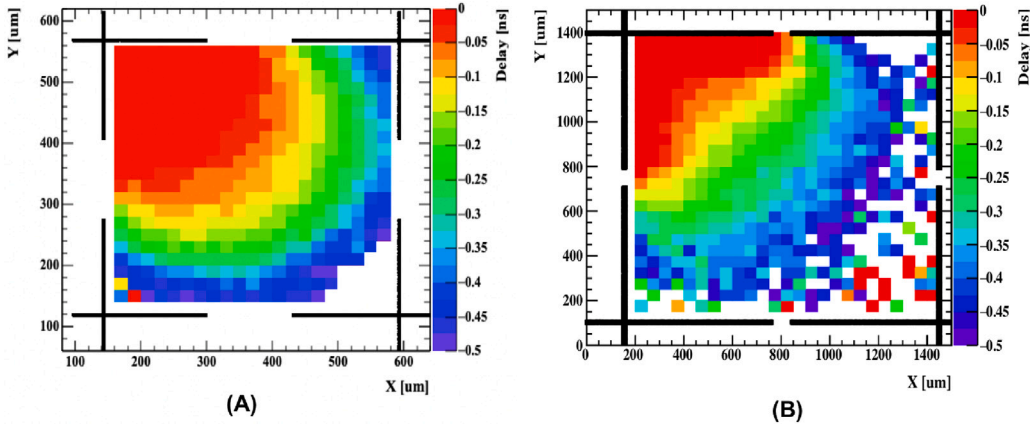

Fig. 9. Signal delay with respect to the top-left read-out pad (A) 450×450 μm^2 structure. (B) 1300×1300 μm^2 structure.

have similar behavior since the best results are obtained for $k_{x,y} \sim 1$. As the pixel pitch gets smaller, the difference between the two methods grows, with SWP performing considerably worse for the smallest pitch.

In the DPC algorithm, the values $k_{x,y} = 0.6, 0.9, 0.85, 0.98$ have been used for the pitch size 200, 340, 450, and 1300 μm, respectively. For the above reasons, in the following of this analysis, the DPC algorithm with signal amplitude will be used.

7.1.3. Determination of the reconstructed coordinates

As seen in Fig. 7(C), the measured coordinates are systematically shifted with respect to their true positions. For a given hit position, this shift ($\Delta x, \Delta y$) can be estimated by comparing the measured and true coordinates in the training dataset, for those events whose reconstructed coordinates are in the proximity (within a circle of r_{cor}) to the hit position under study.

$$\Delta x = \frac{\sum_i^n (x^i_{meas\ training} - x^i_{true\ training}) \times w_i}{\sum_i^n w_i},$$

$$\Delta y = \frac{\sum_i^n (y^i_{meas\ training} - y^i_{true\ training}) \times w_i}{\sum_i^n w_i},$$

$$w_i = \frac{1.}{\sqrt{(x_{meas} - x^i_{meas\ training})^2 + (y_{meas} - y^i_{meas\ training})^2}}$$

(8)

where $(x, y)^i_{true\ training}, (x, y)^i_{meas\ training}$ are respectively the true and measured x, y coordinates of the i training point. The value of r_{cor} does not have a strong impact on the correction, provided it is large enough to include at least a few training positions and not too large to include points that have different migration characteristics. For the present

study, r_{cor} was set to $r_{cor} = 30$ μm. Once $\Delta x, \Delta y$ have been computed, the reconstructed hit coordinates are obtained as:

$$x_{rec} = x_{meas} + \Delta x$$
$$y_{rec} = y_{meas} + \Delta y$$

(9)

7.2. Reconstruction of the hit time

The first significant difference in determining the hit time between RSD and standard UFSD is that in the RSD case, the time measured by a given electrode i, t^i_{meas}, is later than the hit time due to the delay, t^i_{delay}, introduced by the signal propagation on the resistive layer. Therefore, the reconstructed hit time t^i_{rec} can be expressed as:

$$t^i_{rec} = t^i_{meas} + t^i_{delay} + t^i_{setup},$$

(10)

where t^i_{setup} is a hardware-specific offset due to PCB traces and cable lengths.

In [3], the delay has been measured to be about $t_{delay} \sim 0.3$–0.5 ps/μm, dependent on the surface resistivity and sensor capacitance; the devices here measured show a delay per micron as high as ~ 0.7 ps/μm, leading to values of 300–400 ps. Fig. 9 shows the delay maps for the 450×450 μm^2 and 1300×1300 μm^2 structures as measured using the TCT set-up. In these plots, the signal is read out by the top-left electrode, and the colors illustrate the delay. For the 1300 μm^2 structure, when the hit position is near the opposite corner, the signal amplitude is too small to allow determining the arrival time.

The term t^i_{setup} is evaluated experimentally by measuring for each pad i the time of arrival of laser signals shot very near the pad itself.

The second important difference between RSDs and standard UFSDs is that in RSDs there are multiple measurements of the hit time (one
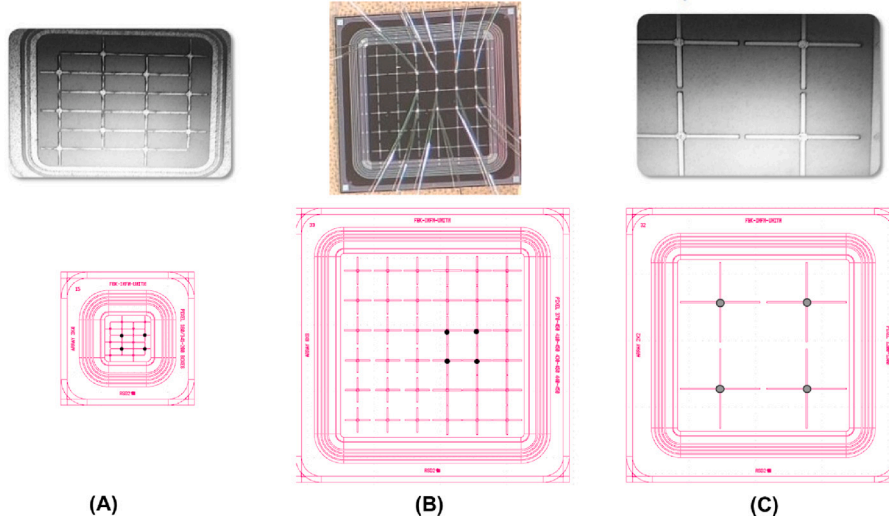
Fig. 10. Structures used in this study. In the bottom row, the pictures are scaled, maintaining the original proportions. The read-out pads delimiting the pixel areas are indicated by the full dots.
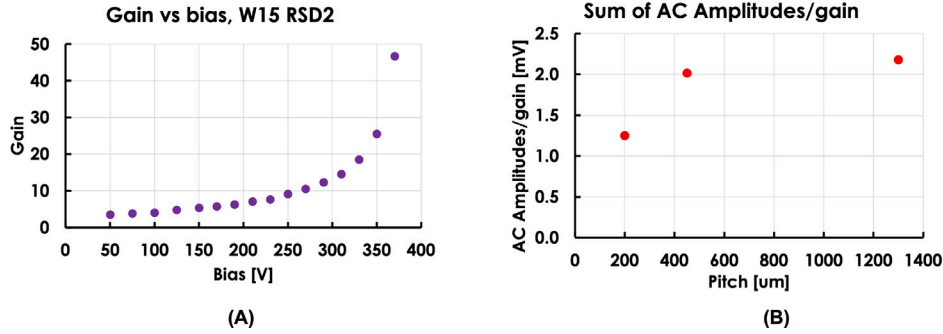

Fig. 11. (A): Gain-voltage characteristics of the sensors used in this analysis. (B): Sum of the four amplitudes of the AC signals divided by the gain. In small pixels, the AC signal is not contained within the four closest read-out pads, so the fraction is lower.

from each read-out pads), and their combination might improve (or deteriorate) the time resolution. The σ_{Landau} does not benefit from multiple measurements, as the signal shape is common to all pads, while the jitter term does. The time of arrival t_{rec} is estimated using the following χ^2 expression:

$$\chi^2 = \frac{\sum_i^4 (t_{rec} - t_{rec}^i)^2}{\sum_i^4 \sigma_i^2},$$ (11)

$$\sigma_i = \frac{\sigma_{el-noise}}{dV_i/dt} \sim \frac{\sigma_{el-noise}}{A_i/t_{rise}},$$

where t_{rec}^i, A_i, and σ_i are the reconstructed hit time, the signal amplitude, and the time jitter measured on pad i, and t_{rise} the signal rise time. Minimizing the χ^2 expression, and dividing out the common factors (t_{rise}, σ_i), the expressions for t_{rec} and its associated error σ_{trec} are found to be:

$$t_{rec} = \frac{\sum_i^4 t_{rec}^i * A_i^2}{\sum_i^4 A_i^2},$$ (12)

$$\sigma_{trec} = \frac{\sigma_{el-noise} * t_{rise}}{\sqrt{\sum_i^4 A_i^2}}.$$

Assuming for simplicity an equal signal split among the four pads, $A_i = A/4$, the expression for the error becomes $\sigma_{trec} = \frac{\sigma_{el-noise} * t_{rise} \sqrt{4}}{A}$, showing that also the time resolution worsens with the number of electrodes n as $\sqrt{n}$.

8. Sensors under study

The structures used in this study are shown in Fig. 10 and their characteristics are listed in Table 1. The only electrodes read out during the measurements are indicated with full dots (while the other electrodes are connected to ground). The smallest sensor, (A), has an active area of $800 \times 800\ \mu m^2$, and has electrodes with arms of different lengths in the x and y directions, 90 μm in x and 165 μm in y. A rectangular pixel of $200 \times 345\ \mu m^2$ is obtained by leaving the electrode internal to the four read-out pads floating. The structures (B) and (C) have an active area of about $2700 \times 2700\ \mu m^2$. The type (B) has a 6 × 6 array of read-out electrodes, with a pitch of 450 μm, while (C) as four read-out pads, defining a single pixel with a pitch of 1300 μm.

The structures have been selected from the same wafer, so they have the same n$^+$ sheet resistivity and gain versus bias behavior, shown in Fig. 11(A). In order to study how the various components of the spatial resolution evolve over a wide signal range, lasers with intensities higher than 1 MIP have been used. For this reason, in the pictures, the gain is reported as "equivalent gain", meaning the product of the gain and the laser setting, expressed in 1-MIP unit.

Fig. 11(B) reports the sum of the amplitudes measured on the four read-out pads divided by the gain of the signal, which is measured on the n^+ resistive layer (in the following called DC-signal) as a function of the pitch. In large structures, 450 μm and 1300 μm pitch, the AC signal is fully (or almost) contained within the four read-out pads, and the ratio does not depend on the pitch. On the other hand, for
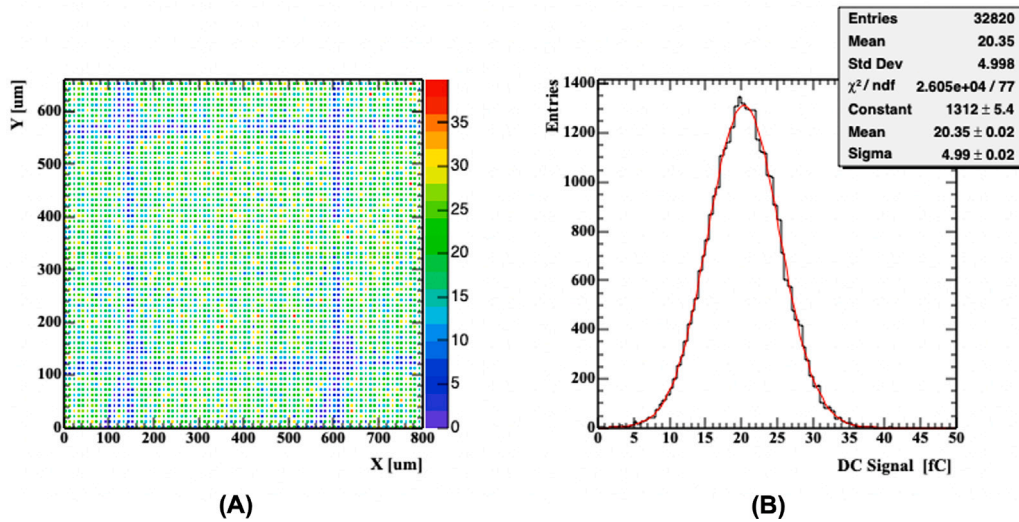
Fig. 12. (A): Area of the DC-signal in fC as a function of position. (B): 1D distribution of the signal charge for shot inside the pixel.
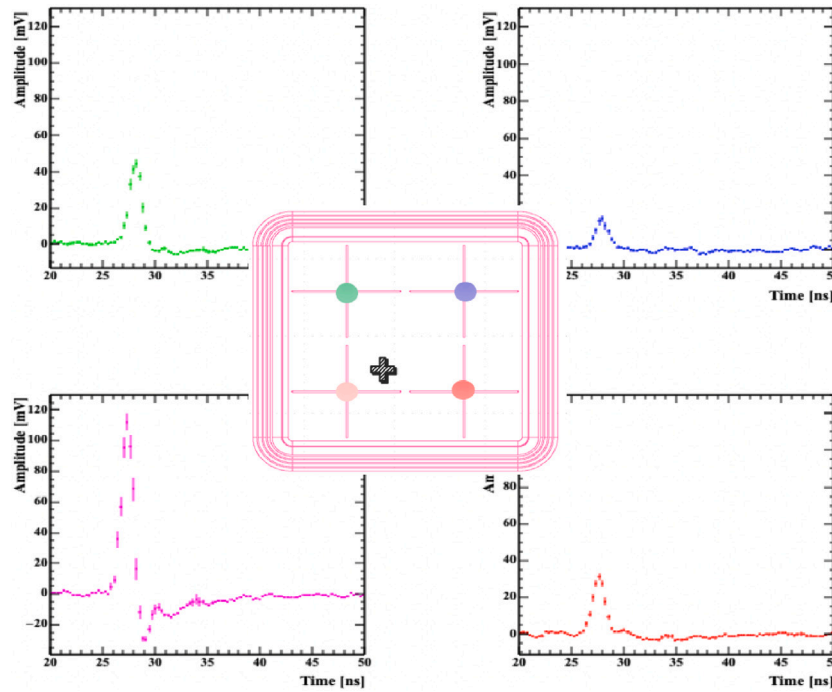

Fig. 13. AC signals on the four read-out electrodes for the 1300 μm pixel structure when the laser is shot at the position indicated by the cross.

the 200×340 μm^2 structure, this ratio is about 40% lower since the signal sharing also involves neighboring pixels, and the signal is not limited to the four closest read-out electrodes. As this analysis uses only four read-out electrodes, the resolution for this smaller structure is degraded.

This observation highlights an important interplay between the n^+ resistivity, the pixel size, and the optimal number of read-out electrodes needed to reconstruct the signal: in order to contain signal sharing to the four electrodes at the pixel corners, the n^+ resistivity should be tuned according to the pixel size, it should be lower for larger pixels and higher for smaller pixels.

8.1. Alignment and signal shape

For each structure under test, the first step is to find the pads coordinates in the laser reference system. This is done by exploiting the fact that the metal of the read-out pads absorbs the laser signal: Fig. 12(A) shows the DC-signal area, in fC, as a function of the laser position for a pixel of 450 μm. The image clearly shows the metal arms of each read-out pad. For the lower two read-out electrodes, the wire bonds are also visible. Fig. 12(B) reports the 1D distribution of the signal charge for the shots inside the pixel. The distribution has a very regular gaussian shape, without long tails. Fig. 13 shows the AC signals
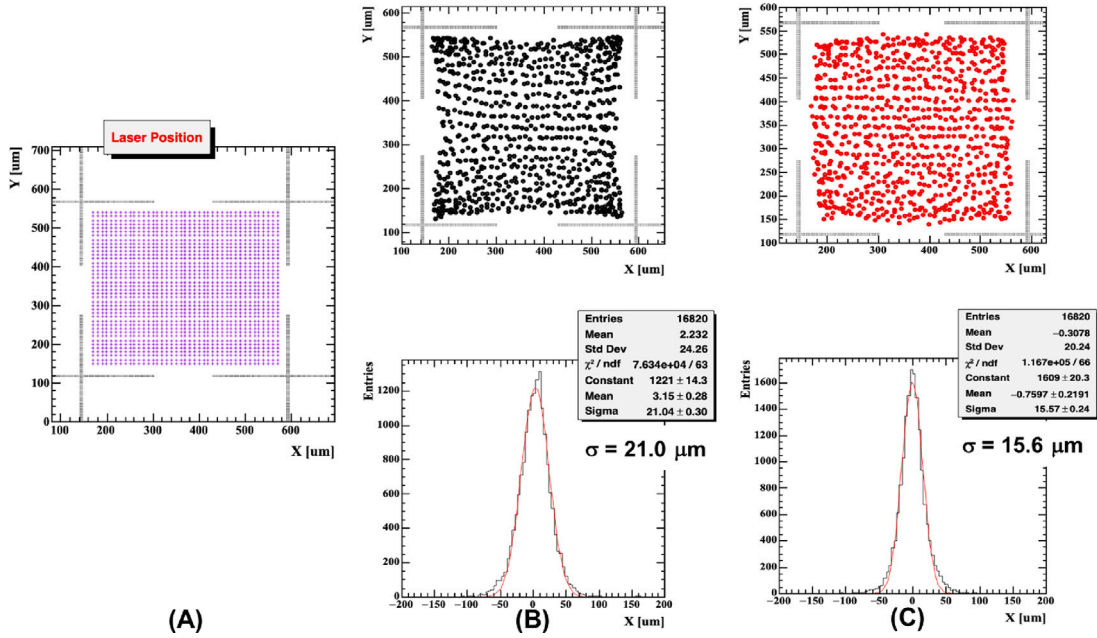
Fig. 14. (A) Position of the laser shots, (B) Uncorrected position reconstruction, (C) Corrected position reconstruction.
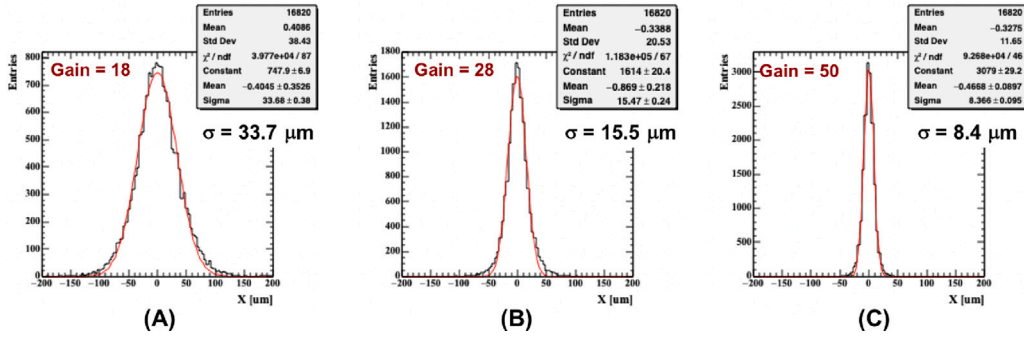

Fig. 15. Spatial resolution as a function of the RSD gain (18, 28, 50) for the 450 × 450 μm² structure. The corresponding collected charge, read by the DC electrode, for each gain is 9, 14 and 25 fC respectively. In these measurements, the two terms $\sigma_{setup}, \sigma_{sensor}$ are zero.

on the four read-out electrodes for the 1300 μm pixel structure when the laser is shot at the position indicated by the cross.

The signals are very fast, about 2 ns long, and are not distorted even by a rather long propagation, about 1 mm for the green, blue, and red signals. The opposite polarity lobe of the signal is quite small, indicating a fairly long RC time constant. More details on signal propagation and the evaluation of the RC time constant can be found in [3].

9. Evaluation of the spatial resolution

In the following, the spatial resolution for a given device is estimated as a function of the gain. As the migration matrix has been measured on the device under test, the terms σ_{setup} and σ_{sensor} of Eq. (1) are by construction equal to zero. An estimate of these two terms is provided in Section 9.2.

For each sensor, at every biasing point, the following steps are performed:

- The laser is shot in a grid of points covering the pixel area. The step size is 10 μm for the 200 × 340 μm² and 450 × 450 μm² structures, while it is 20 μm for the 1300 × 1300 μm² structure. This is illustrated on Fig. 14(A).

- The hit positions are reconstructed using Eq. (6): Fig. 14(B upper plot) shows these reconstructed positions for the 450 × 450 μm² structure. Thanks to the read-out electrode design, the resolution, reported in Fig. 14(B bottom plot), is quite good, $\sigma_{hit\,pos}$ = 21.0 μm. Small non-gaussian tails are visible due to the clustering of the reconstructed positions near the electrodes.

- The reconstructed positions are corrected using the procedure outlined in Section 7. The position of the laser shots is required to be at least 30 μm away from the metal strips of the read-out pads in order to assure that the laser has not been inadvertently attenuated. The effect of the correction can be gauged by comparing Fig. 14(B) and (C): the distortion in the reconstruction is almost completely eliminated, and the corrected points form a more regular grid. The position resolution improves, from $\sigma_{hit\,pos}$ = 21.0 μm to $\sigma_{hit\,pos}$ = 15.6 μm, since the accuracy of the reconstruction becomes much better (smaller σ_{rec}) and the terms σ_{setup} and σ_{sensor} are eliminated by the correction.

The evolution of the spatial resolution with gain for the 450 × 450 μm² structure is shown in Fig. 15. Gain 18 (A) and 28 (B) were obtained with the laser set to generate one MIP, while, for gain 50 (C), the laser was set to generate about two MIPs. For all values of gain,
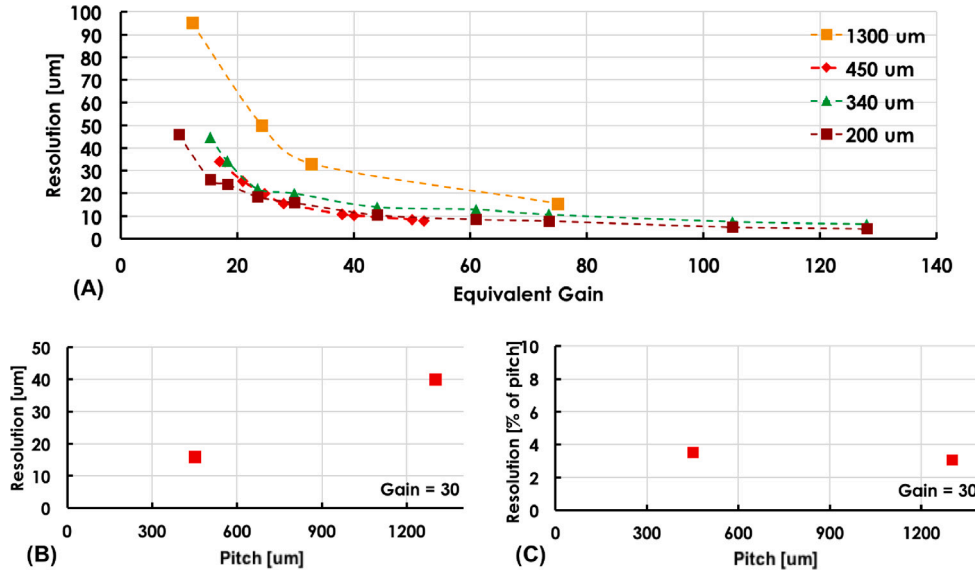
Fig. 16. (A) The spatial resolution versus gain for the four pitch sizes analyzed. For the two largest structures: (B) Spatial resolution versus the pitch size, (C) Spatial resolution, expressed as a percentage of the pitch size, versus pitch size. In these measurements, the two terms $\sigma_{setup}, \sigma_{sensor}$ are zero.
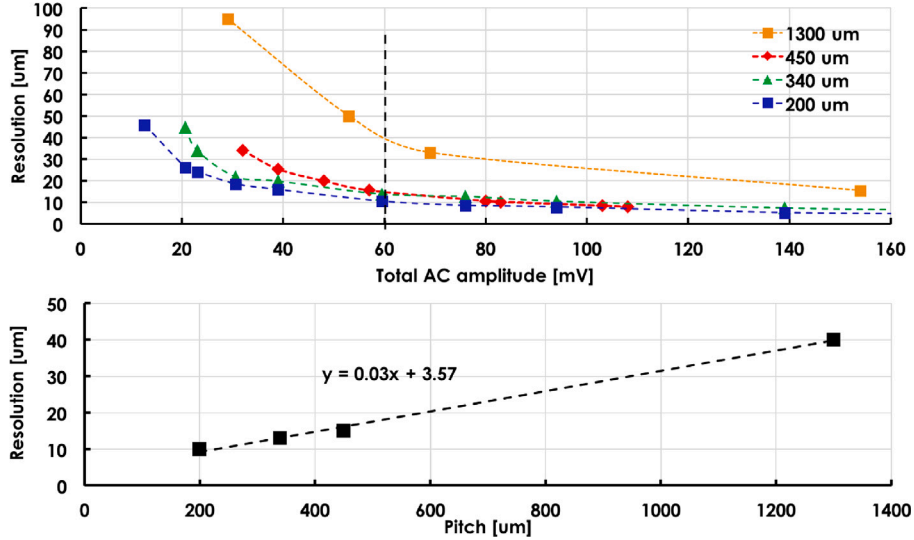

Fig. 17. Top: Spatial resolution as a function of total amplitudes. Bottom: Spatial resolution versus pitch size when the total AC amplitude equals 60 mV. As predicted by Eq. (2), at a fixed amplitude, the resolution depends linearly on the pixel size. In these measurements, the two terms $\sigma_{setup}, \sigma_{sensor}$ are zero.

the non-gaussian tails are very small, indicating that the correction procedure works correctly.

9.1. Results

The spatial resolution as a function of gain for the different sensor types is presented in Fig. 16(A). The resolutions for the 200 and 340 μm pitches are not as good as they could be since, as anticipated in Section 8, the signal is not contained in the four read-out pads. For the two largest structures, at gain 30, Fig. 16(B) reports the spatial resolution versus the pitch size, while Fig. 16(C) expresses the spatial resolution as a percentage of the pitch. A spatial resolution of about 3% of the pitch size is achieved at gain 30.

The top plot in Fig. 17 shows the spatial resolution as a function of the total AC amplitude, defined as the sum of the amplitudes measured on the four read-out electrodes. As expected, for equal signal amplitude, the smaller pitch sizes perform better. The bottom plot reports the spatial resolution as a function of the pitch at amplitude = 60 mV (about

gain = 30). At fixed amplitude, the resolution scales linearly with the pixel size, as it should happen when the resolution is dominated by the jitter contribution, estimated from the model in Eq. (2). The fit indicates a resolution of 3% the pixel size with an offset of 3.5 μm.

Fig. 18 compares the resolution of each pitch size with the jitter contribution. Even though the only degree of freedom of the calculated jitter curves is a common normalization parameter, the agreement with the experimental data is quite good.

9.2. Evaluation of the $\sigma_{setup}^2 + \sigma_{sensor}^2$ terms

In the results presented above, the migration matrix minimizes the term σ_{rec} and removes the combined contributions of $\sigma_{setup}^2 + \sigma_{sensor}^2$ since it is computed on the same pixel used for the analysis. An estimate of $\sigma_{setup}^2 + \sigma_{sensor}^2$ for the present study can be evaluated by rotating the migration map, for example, by 180°. With this operation, possible differences arising from the TCT set-up, read-out amplifiers, and non-uniformity of the sensor sharing quality (for example, non-uniform
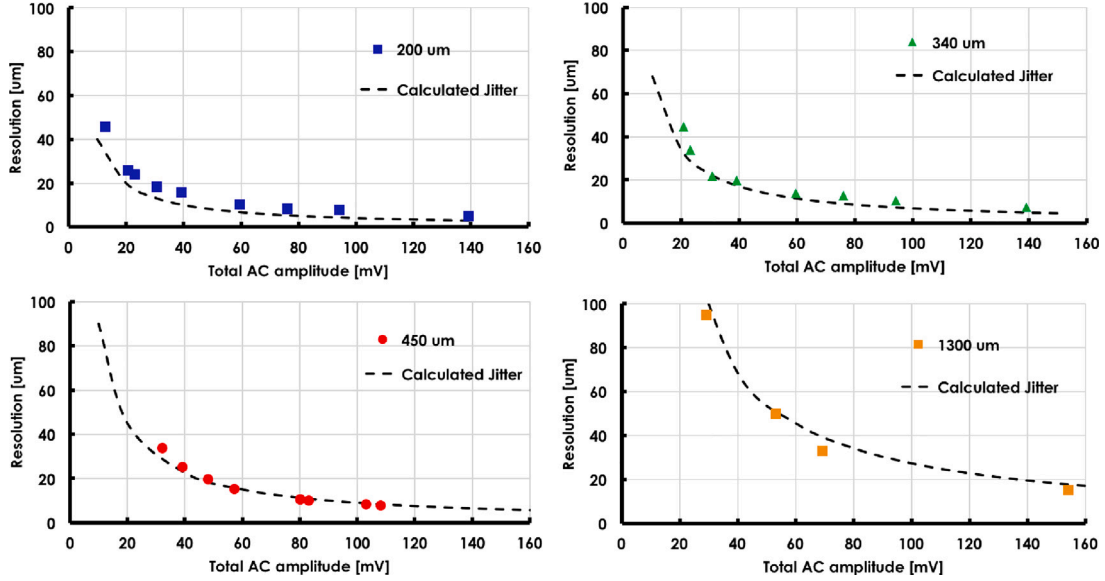
Fig. 18. Spatial resolution as a function of the total AC amplitude for each pitch size and the calculated jitter contribution. In these measurements, the two terms $\sigma_{setup}, \sigma_{sensor}$ are zero.

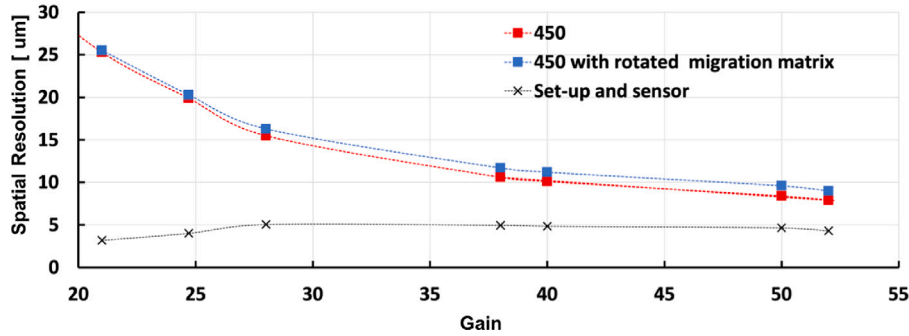**Fig. 19.** Spatial resolution as a function of gain for the 450 × 450 μm² structure. The red squares were obtained with the standard procedure, while for the empty blue squares the migration map was rotated by 180°. The cross markers show the difference (in quadrature) between the blue and red squares.

resistivity or oxide thicknesses) are enhanced since the migration patterns of the points on the left (top) of the pixel center are applied to the points on the right (bottom) and vice versa. Fig. 19 shows the resolution as a function of the gain for the 450 μm pitch pixel obtained by applying the standard and the 180° rotated migration matrix. Using the rotated migration matrix, the resolution is always slightly worse, and the difference in quadrature of the two resolutions is fairly constant and equal to about 5 μm (black dotted line with cross markers).

The same analysis performed on the 1300 μm structure leads to a value of $\sigma_{setup}^2 + \sigma_{sensor}^2 \sim 4.5$ μm, while the use of the rotated migration matrix on the 200 × 340 μm² structure leads to values of spatial resolution compatible with the standard matrix.

10. Evaluation of the time resolution

This study was performed using the TCT set-up, measuring the difference between the trigger time and reconstructed event time t_{rec} of laser shots distributed over the whole pixel surface.

Fig. 20(A) shows the quantity $t_{trig} - t_{rec}$, with the latter obtained combining the time measured by the four pads, as a function of the hit position for the 450 × 450 μm² structure, while (B) shows the 1D distribution.

The 2D map shows a very good uniformity over the whole surface, especially considering that this pixel is quite large. This consideration is strengthened by the 1D distribution shown on (B): the tails are due

to events concentrated near the pixel corners. In this analysis, the best results have been obtained using as t_{meas}^i the time of the maximum (from a gaussian fit on the five highest samples) and not the value corresponding to the more common constant fraction algorithm. This feature is linked to the limited number of samples on the signal rising edge (the digitizer has a 5 GS/s sampling rate) and not to a specific aspect of the resistive read-out.

Overall, these results show that resistive read-out does not degrade the timing performance of the UFSD design and that very uniform response over large pixels is achievable.

10.1. Results

The complete set of measurements for the three RSD structures is shown in Fig. 21. The trigger resolution, evaluated at 10 ps, has been subtracted in quadrature. The resolution is presented as a function of the total AC amplitude. The plot also shows the calculated jitter term contributing to the time resolution: the values measured are in good agreement with the jitter term. It is important to stress the following points:

- Since a laser shot creates uniform charge deposition, in this study the term σ_{Landau} is absent. This contribution has been measured [3] to be around 30 ps for a 50 μm thick RSD sensor.
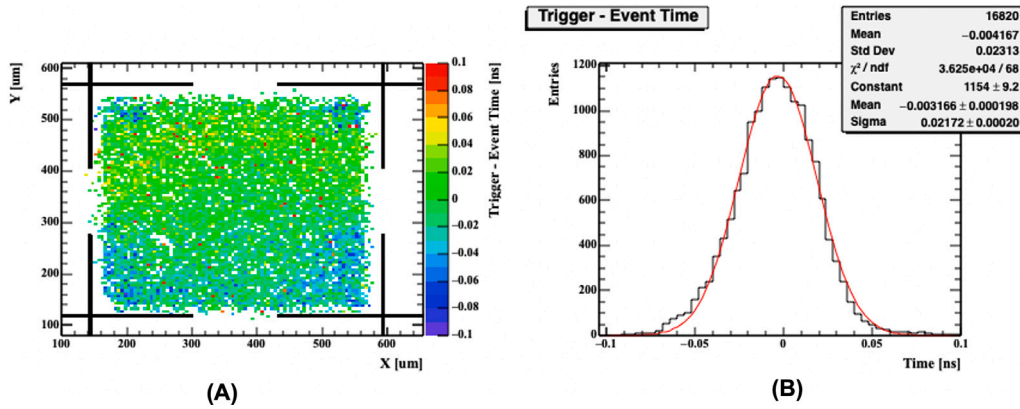
Fig. 20. Time difference between the trigger and the reconstructed event time (A) on the pixel surface (B) 1D distribution.
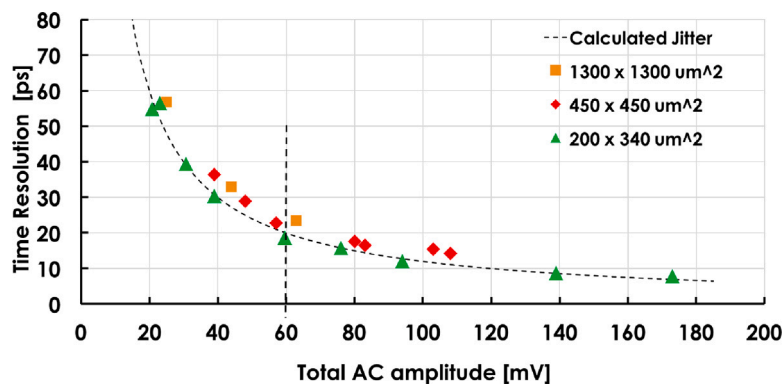

Fig. 21. Time resolution as a function of the total AC amplitude. Results obtained with a laser TCT system ($\sigma_{Landau} = 0$ ps).
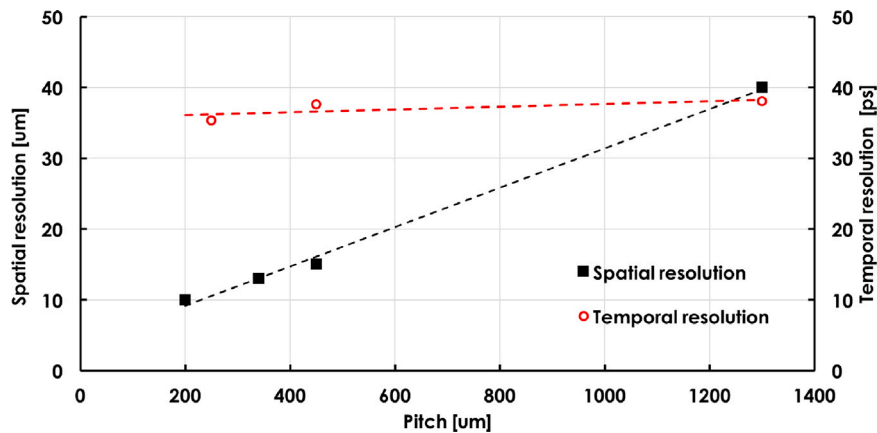

Fig. 22. Space and time resolutions for the structures under test when the sum of the AC amplitudes is 60 mV (gain = 30).

- Given the excellent spatial resolution, the term σ_{delay} is subleading with respect to σ_{jitter}, as can be seen in the plot.

Therefore, the time resolution is dominated by the jitter contribution. One feature is particularly striking: the points align quite well along the curve representing the jitter contribution, regardless of the pixel size. This indicates that the jitter depends mostly upon the total AC amplitude, and it is not spoiled by the propagation on the n$^+$ resistive surface.

Assuming to work at a total AC amplitude of 60 mV (gain = 30), a time resolution of about 19 ps is achieved for the 200×340 µm^2 structure, and of 23 ps for both the 450×450 µm^2 and 1300×1300 µm^2 structures.

11. Extrapolated performance of RSD sensors with MIP

The extrapolated resolutions for the determination of the position and time coordinates, for the sensors under test, are presented in Fig. 22. The time resolution has been computed by adding the Landau noise term ($\sigma_{Landau\ noise} = 30$ ps) in quadrature to the time jitter term while the spatial resolution by adding $\sigma_{setup}^2 + \sigma_{sensor}^2 = 5$ µm in quadrature to the spatial term of the 450 and 1300 µm structures.

- The spatial resolution is about 3% of the pixel size, and it scales linearly with the pixel size, as predicted by Eq. (1)
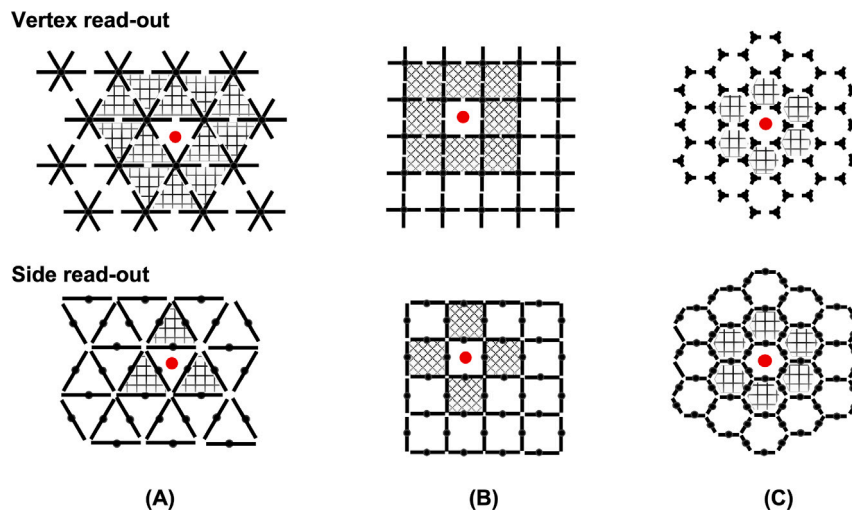- The temporal resolution is fairly constant at about 38 ps as a function of the pixel size.

Vertex read-out

Side read-out

(A)   (B)   (C)

Fig. 23. Possible pixel shapes (triangle, square, and hexagon) and read-out electrode layouts (at the vertexes or at the sides). The most accurate resolution is obtained when the area around the hit (shown as checkered) is not hit by a second particle.

These results demonstrate that RSD sensors with cross-shaped electrodes are able to achieve excellent resolutions in the determination of the position and time coordinates, over a very large range of pixel sizes.

12. Resolution, occupancy, and power consumption for different RSD pixel shapes

In this section, a comparison among possible alternative pixel shapes (triangular, square, and hexagonal) and read-out electrode layouts (located at the vertexes - "vertex read-out"- or along the sides of a cell - "side read-out") is presented. These layouts are shown in Fig. 23.

The most accurate resolution is obtained when the pixels around the impact point (red dot) are not hit by additional particles. For this reason, the determination of the optimum pixel size when using RSD sensors should not be based solely on the spatial resolution but also on the sensor occupancy. As a general rule, power consumption (i.e. the number of read-out amplifiers) is minimized by using vertex electrodes. The very same choice maximizes the area that needs to be without additional particles, for obtaining the best position resolution: optimized reconstruction algorithms could lead to good performance even in case of a second hit in the area covered by the same electrodes.

13. Conclusions

This paper presents a detailed evaluation of the space and time resolutions of 50 μm thick RSD sensors with cross-shaped electrodes, manufactured at FBK as part of the RSD2 production. The studies, performed using a laser TCT setup, allow to estimate the performance of the sensors with charged particles, demonstrating the concurrent excellent space and time resolution over a large range of pixel sizes, from 200 μm to 1300 μm.

At gain = 30, the time resolution for all structures is between 35–40 ps, dominated by the Landau noise term, while the space resolution is about 3% of the pitch size, dominated by the jitter term. For equal spatial resolution, the RSD design reduces the number of read-out channels by about 50–100 with respect to sensors employing single-pixel read-out: this is a crucial feature to limit power consumption and to provide more space to fit the electronic circuits.

This analysis also demonstrates that the n^+ resistive layer non-uniformity of the FBK RSD sensors is small and has a limited impact on the performance.

Declaration of competing interest

The authors declare that they have no known competing financial interests or personal relationships that could have appeared to influence the work reported in this paper.

Data availability

Data will be made available on request.

References

[1] The ATLAS Collaboration, et al., The ATLAS experiment at the CERN large hadron collider, J. Instrum. 3 (08) (2008) S08003, http://dx.doi.org/10.1088/1748-0221/3/08/s08003.

[2] W. Adam, et al., The cms phase-1 pixel detector upgrade, J. Instrum. 16 (2021) P02027.

[3] M. Tornago, et al., Resistive AC-coupled silicon detectors: principles of operation and first results from a combined analysis of beam test and laser data, Nucl. Inst. Meth. A 1003 (2021) 165319, http://dx.doi.org/10.1016/j.nima.2021.165319, arXiv:2007.09528.

[4] H. Sadrozinski, A. Seiden, N. Cartiglia, 4D tracking with ultra-fast silicon detectors, Rep. Progr. Phys. 81 (2017) 026101, http://dx.doi.org/10.1088/1361-6633/aa94d3.

[5] M. Mandurrino, et al., Demonstration of 200-, 100-, and 50- μm pitch resistive AC-coupled silicon detectors (RSD) with 100% fill-factor for 4D particle tracking, IEEE Electr. Device L. 40 (11) (2019) 1780, http://dx.doi.org/10.1109/LED.2019.2943242.

[6] F. Siviero, et al., First application of machine learning algorithms to the position reconstruction in resistive silicon detectors, J. Instrum. 16 (03) (2021) P03019, http://dx.doi.org/10.1088/1748-0221/16/03/p03019.

[7] R. Arcidiacono, et al., High-accuracy 4D particle trackers with resistive silicon detectors (AC-LGADs), J. Instrum. 17 (03) (2022) C03013, http://dx.doi.org/10.1088/1748-0221/17/03/c03013.

[8] Particulars, advanced easurement systems, http://particulars.si.

[9] A. Apresyan, et al., Measurements of an AC-LGAD strip sensor with a 120 GeV proton beam, J. Instrum. 15 (2020).

[10] S. Siegel, R. Silverman, Y. Shao, S. Cherry, Simple charge division readouts for imaging scintillator arrays using a multi-channel pmt, IEEE Trans. Nucl. Sci. 43 (3) (1996) 1634–1641, http://dx.doi.org/10.1109/23.507162.